RSC Advances

ROYAL SOCIETY OF CHEMISTRY

www.rsc.org/advances

RSCPublishing

ARTICLE

Hierarchical $CuCo_2O_4$ Nanowire@$NiCo_2O_4$ Nanosheet Core/Shell Arrays for High-Performance Supercapacitors

Kang Zhang[1], Wei Zeng[2], Guanhua Zhang[3], Sucheng Hou[3], Fei Wang[5], Taihong Wang[3,4] , Huigao Duan[3,4] *

1. School of Materials Science and Engineering, 2. School of Chemistry and Chemical Engineering, 3. School of Physics and Electronics, 4. State Key Laboratory for Chem/Biosensing and Chemometrics, Hunan University, Hunan, 410082 P. R. China. 5. College of Science, National University of Defense Technology. Hunan, 410073 P.R. China.
*E-mail: duanhg@hnu.edu.cn

Ternary metal oxides have attracted extensive attentions for supercapacitor applications due to their enhanced performance compared to their binary counterparts. In this work, 3D $CuCo_2O_4$@$NiCo_2O_4$ core/shell nanostructures have been synthesized via a two-step method on nickel foam followed by a post annealing process. Morphological characterizations show that the porous $CuCo_2O_4$ nanowires are well covered by $NiCo_2O_4$ nanosheets. The hybrid electrode is used as a binder-free electrode, showing a high specific capacitance of 2029 F g^{-1} (while the areal capacitance is 2.59 F cm^{-2}) at the current density of 10 mA cm^{-2}, higher than the $CuCo_2O_4$ electrode. After 4500 cycles, the specific capacitance remains 1548 F g^{-1}, ~80% of the original capacitance. In particular, the hybrid electrode exhibits great rate capability, the hybrid electrode retains 1551 F g^{-1} as the current density increases to 30 mA cm^{-2}, which can be ascribed to the excellent electron transport properties of core/shell $CuCo_2O_4$@$NiCo_2O_4$ structures.

1. Introduction

With the rapid development of electric vehicles and portable devices, there is an urgent need for electrochemical energy storage. Compared to lithium-ion batteries, supercapacitors (SCs) have attracted extensive interest due to their higher power densities, fast charge rate and long cycle life. In general, SCs can be divided into two types defined by the storage mechanism, i.e., electrical double layer capacitors (EDLCs) and pseudocapacitors (PCs). Specifically, EDLCs store the charged ions from an electrolyte onto electrodes forming a double layer structure via a physically adsorbing-desorbing process. Current commercial capacitors mainly belong to EDLCs, which based on carbonaceous materials including carbon aerogel,[1, 2] carbon fiber,[3] carbon nanotube and graphene.[4-8] However, EDLCs have suffered from the low energy density which restricts its extensive applications. On the contrary, PCs can provide much higher energy density due to their fast and reversible faradic redox reactions. Therefore, much more attentions have been focused on the study of PCs recent years.

Seeking for better electrode materials is essential to develop PCs. Transition metal oxides,[9-11] hydroxides[12-14] and sulfides[15-17] have been widely reported for PCs owing to their high theoretical capacity, low cost and environmental compatibility. Among the transition metal oxides, Co_3O_4 has become a promising electrode material because of its high theoretical capacity.[11, 18-22] However, the relatively low conductivity and high cost restrict its commercial application. In order to overcome these disadvantages and realize better electrochemical performance, some attempts have been made to synthesize ternary oxide via replacing Co in Co_3O_4 partially with alternative metals (e.g., Zn, Cu, Ni, Mn, and Fe).[23-29] Bao et al. synthesized mesoporous $ZnCo_2O_4$ nanosheet arrays on Ni foam via a simple hydrothermal method with a ultrahigh specific pseudo-capacitance of 2468 F g^{-1} at 5 A g^{-1} and excellent cycling stability.[24] Chen and co-workers fabricated porous $NiCo_2O_4$ flowerlike nanostructures by a simple hydrothermal and subsequent annealing process with an enhanced specific capacitance of 658 F g^{-1} at 1 A g^{-1} compared to Co_3O_4.[25] Obviously, ternary metal oxides which possess multiple oxidation states exhibit a higher supercapacitive performance in comparison with their binary counterparts.

Besides, in order to further enhance the electrochemical ability, lots of electrode materials with hierarchical core/shell nanostructure have been investigated.[23, 30-36] In a typical

core/shell system, the core can provide better conductivity for charge transfer, while the shell can serve as active electrode materials with high surface areas. As a result, researchers have demonstrated that such core/shell nanostructure can realize a higher electrochemical performance due to the synergistic effect. For instance, Huang et al. have shown that hybrid composites $Ni(OH)_2$@$NiCo_2O_4$ exhibited a notable increased capacitance and good cycle performance compared with a pristine $Ni(OH)_2$ array.[31] In addition, the materials grown on substrate can be directly used as electrode for SCs without using a polymer binder, which can improve the ion diffusion and electron conductivity. Then the better electrochemical performance can be realized.[37, 38] Qian and co-workers synthesized the ultralight, high-surface-area, multifunctional graphene-based aerogels as binderless monolithic electrodes for supercapacitors with a good electrochemical performance. Yu group reported the free-standing Co-$Co(OH)_2$ composite nanoflakes on 3D nickel foam for supercapacitors, which exhibited a high specific capacitance.

On the basis of the above considerations, we designed and synthesized a hierarchical core/shell structure of $CuCo_2O_4$ nanowires@$NiCo_2O_4$ nanosheets on Ni foam in this work. We used thin $CuCo_2O_4$ nanowires as the scaffold cores to deposit the "shell" composed by $NiCo_2O_4$ nanosheets. Taking the advantage of the synergistic effect and 3D core/shell nanostructure, the hybrid electrode exhibited a notable increased electrochemical performance with a high specific capacitance of 2029 F g^{-1} at the current density of 10 mA cm^{-2} and an excellent rate capability (61.6% capacity retention at 30 mA cm^{-2}). Moreover, the hybrid electrode retains 76% of the original capacity after 4500 cycles at 10 mA cm^{-2}, which indicates an excellent cycling stability.

2. Experimental

Materials synthesis

All the reagents used in the experiment were analytical grade (purchased from Sinopharm) without further purification. The Ni foam was cleaned by sonication in acetone, ethanol, and deionized (DI) water in sequence for 30 min, respectively.

Synthesis of $CuCo_2O_4$ nanowires arrays (NWAs). In a typical procedure, 0.474 g of $CoCl_2$, 0.171 g of $CuCl_2$, and 0.54 g of urea were dissolved in 30 mL distilled water under constant magnetic stirring. After being stirred for 30 min, the as-obtained solution and Ni foam were transferred into a 50 mL Teflon-lined stainless steel autoclave. The autoclave was sealed and maintained at 120℃ for 6 h in an electric oven and then cooled down to room temperature naturally. The obtained sample was collected and washed by distilled water and absolute alcohol several times. Finally, the sample was put into a quartz tube and annealed at 300℃ for 2 h in flowing nitrogen (50 sccm), thus the final sample was obtained.

Synthesis of $CuCo_2O_4$@$NiCo_2O_4$ hybrids (NWSAs). The $CuCo_2O_4$@$NiCo_2O_4$ arrays were synthesized by the electrodeposition of $NiCo_2O_4$ nanosheets on the surface of $CuCo_2O_4$ NWAs. The co-electrodeposition was performed in a standard three-electrode glass cell at the room temperature, including a Ni foam supported $CuCo_2O_4$ arrays as the working electrode, a Pt foil as the counter-electrode and saturated calomel electrode (SCE) as the reference electrode. The electrochemical synthesis of $NiCo_2O_4$ was performed in a $Co(NO_3)_2 \cdot 6H_2O$ (4mM) and $Ni(NO_3)_2 \cdot 6H_2O$ (2mM) mixture by the cyclic voltammetry (CV) method for 30 cycles. The CV deposition was conducted in the potential range from -0.6 to -1.2V with a sweep rate of 20 mV s^{-1} using a CHI660e electrochemical workstation. The CVs of the electrodeposition was shown in Figure S1. The as-prepared sample was taken off and rinsed with distilled water. Finally the sample was put into a quartz tube and annealed at 300℃ for 2 h.

The mass of the samples was weighed by an electronic balance with an accuracy of 0.001mg. The mass of the pure Ni foam, $CuCo_2O_4$ NWAs on Ni foam after hydrothermal process, and $CuCo_2O_4$@$NiCo_2O_4$ on Ni foam after eletrodeposition were noted as M_1, M_2, and M_3, respectively. The mass of $CuCo_2O_4$ NWAs (noted as M_4) was calculated via the following formulas:

$$M_4=M_2-M_1, \quad (1)$$

and the mass of $CuCo_2O_4$@$NiCo_2O_4$ (noted as M_5) was calculated to be:

$$M_5=M_3-M_1, \quad (2)$$

Characterizations

The morphology of as-prepared samples was characterized by scanning electron microscopy (SEM, Hitachi S-4800). Transmission electron microscope (TEM) images, high-resolution transmission electron microscopy (HRTEM) images were obtained with JEM-2100F equipped with Oxford X-Max80 EDS detector. The crystallographic phases of the $CuCo_2O_4$ nanowire@$NiCo_2O_4$ nanosheet core/shell arrays were observed by X-ray diffraction spectroscopy (XRD Rigaku 2550).

Electrochemical measurements

The electrochemical tests were carried out in a three electrode electrochemical cell containing 3 M KOH aqueous solution as the electrolyte. The as-prepared sample was directly used as the working electrode. A saturated calomel electrode (SCE) was used as the reference electrode and a platinum electrode as the counter electrode. The area of the working electrode was made about 1 × 1 cm^2. According to the equation (1) and (2), the mass loading of $CuCo_2O_4$ on Ni foam was 0.98 mg cm^{-2} and the mass loading of $CuCo_2O_4$@$NiCo_2O_4$ hybrid was 1.28 mg cm^{-2}. The cyclic voltammetry (CV) measurements and galvanostatic charge–discharge measurements were carried out with an electrochemical workstation (CHI 660e). Electrochemical impedance spectroscopy (EIS) measurements were performed by applying an AC voltage with 1 mV amplitude in a frequency ranging from 0.01 Hz to 100 kHz at open circuit potential. The areal capacitance (C_a) and specific capacitance (C_s) were calculated by following equations:

$$C_s = \frac{It}{mV} \quad (3)$$

$$C_a = \frac{It}{SV} \quad (4)$$

Where m is the mass (g) loading of electrode material on Ni foam, S is the geometrical area (cm^2) of the working electrode, V is the potential window (V), I represents the discharge current (A) and t is discharge time (s).

3. Results and discussion

As schematically shown in Figure 1, the unique hierarchical core/shell structure of $CuCo_2O_4$ NWs@$NiCo_2O_4$ NSs on Ni foam was synthesized via two-step method with a post-annealing process.

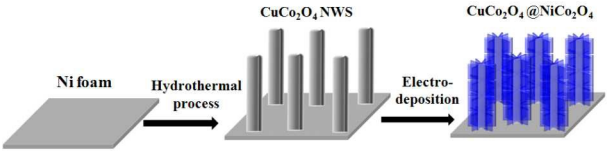

Figure 1. Schematic illustration of the fabrication process of 3D hybrid hierarchical $CuCo_2O_4$ nanowire@$NiCo_2O_4$ nanosheet core/shell arrays on Ni foam.

In this paper, 3D porous Ni foam was used as the substrate. The low-magnification SEM image of Ni foam was shown in Figure 2a. First, the $CuCo_2O_4$ nanowire arrays were grown on Ni foam by a facile hydrothermal and post-annealing process. Figure 2b shows the close-up image of the interface between the Ni foam and $CuCo_2O_4$ nanowires. Figure 2c and 2d shows the scanning electron microscopy (SEM) images of the $CuCo_2O_4$ nanowires on Ni foam. It is obvious that the Ni foam is covered by the $CuCo_2O_4$ nanowires uniformly with an average diameter of ~100 nm and length of ~4 μm. Then, the $CuCo_2O_4$ nanowire arrays grown on Ni foam were used as the scaffold for the electrodeposition of $NiCo_2O_4$ nanosheets, while the $NiCo_2O_4$ nanosheets served as the "shell". The $CuCo_2O_4$ nanowires can provide a vast quantity of sites for the growth of $NiCo_2O_4$ nanosheets. Figure 2e and 2f shows the SEM images of the $CuCo_2O_4$@$NiCo_2O_4$ core/shell arrays. Obviously, the surface of $CuCo_2O_4$ nanowires becomes rough and covered by ultrathin $NiCo_2O_4$ nanosheets after the electrodeposition process. As shown in Figure 2f, the obtained $CuCo_2O_4$@$NiCo_2O_4$ core/shell arrays are well aligned on Ni foam. The $CuCo_2O_4$ nanowire arrays are partially covered by the interconnected $NiCo_2O_4$ nanosheet shells, which means that both the "core" and the "shell" can take part in the redox reaction during the charge/discharge process. Typically, core/shell arrayed structures can enhance the surface areas, providing more electrochemical active sites to boost the area capacitance during the reversible redox reaction.

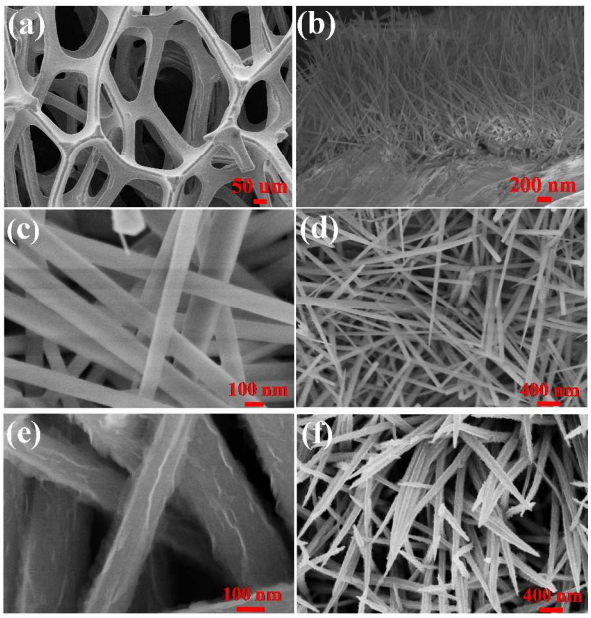

Figure 2. SEM images of the fabricated structures. (a) Low-magnification SEM image of Ni foam. (b) The close-up image of the interface between the Ni foam and $CuCo_2O_4$ nanowires. (c and d) Bare $CuCo_2O_4$ nanowire arrays under different magnification. (e and f) $CuCo_2O_4$ nanowire@$NiCo_2O_4$ nanosheet core/shell arrays under different magnification.

XRD was used to investigate the structural properties of the fabricated structures. To avoid the strong XRD signal of Ni foam substrate, the $CuCo_2O_4$ and $CuCo_2O_4$@ $NiCo_2O_4$ were synthesized on carbon cloth for XRD. The successful preparation of $CuCo_2O_4$ on carbon cloth was confirmed by XRD. As shown in Figure S2 (a), all the diffraction peaks can be well indexed to the $CuCo_2O_4$ phase (JCPDS no. 1-1155) except the XRD signal resulted from carbon cloth. Similarly, the X-ray diffraction was used to confirm the composition of $CuCo_2O_4$@$NiCo_2O_4$. As shown in Figure S2 (b), all the diffraction peaks can be well indexed to the $CuCo_2O_4$ phase (JCPDS no. 1-1155) and the spinel $NiCo_2O_4$ phase (JCPDS 73−1702).

In order to further verify the structural properties of $CuCo_2O_4$ and $NiCo_2O_4$, the detailed microstructure and morphology of $CuCo_2O_4$ and $CuCo_2O_4$@$NiCo_2O_4$ hybrid electrode were analyzed by high-resolution transmission electron microscopy (HRTEM). Figure 3a shows the low-magnification TEM image of as-prepared $CuCo_2O_4$ nanowires, demonstrating that the $CuCo_2O_4$ nanowires are highly porous structures. Besides, according to the Figure 3b, the image of selected area electron diffraction (SAED) pattern indicates a good crystallinity of $CuCo_2O_4$. Furthermore, the fringe spacing is measured to be 0.28 nm, which is well corresponding to the (220) plane of the spinel $CuCo_2O_4$. The SAED result is well consistent with the previous XRD results. Figure 3c shows the typical TEM image of $CuCo_2O_4$@$NiCo_2O_4$ hybrid electrode. Obviously, the highly porous $CuCo_2O_4$ nanowires are covered by a $NiCo_2O_4$ nanosheet layer, forming a unique core/shell

nanostructure. It is worth noting that some of the nanosheets might be damaged during the sonication process for preparing the TEM sample. As shown in Figure 3d, the selected area electron diffraction (SAED) pattern indicates the polycrystalline characteristic of the $NiCo_2O_4$ nanosheets. In addition, the fringe spacing is measured to be 0.24 nm, which is well corresponding to the (311) plane of the spinel $NiCo_2O_4$ and in accordance with the XRD data.

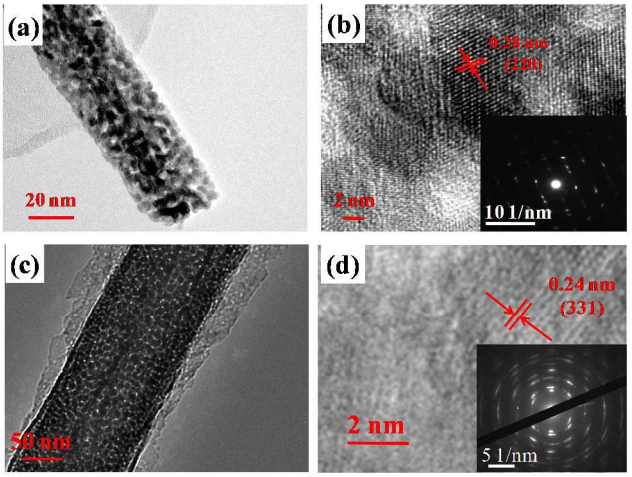

Figure 3. (a) and (c) TEM images of pristine $CuCo_2O_4$ and $CuCo_2O_4$@$NiCo_2O_4$ hybrid electrode. (b) and (d) HRTEM image and the corresponding SAED pattern of pristine $CuCo_2O_4$ and $CuCo_2O_4$@$NiCo_2O_4$ core/shell arrays respectively.

The "oriented attachment" and "selfassembly" processes, involving a spontaneous self-organization between neighboring particles to share a common crystallographic orientation, dominated the growth of $CuCo_2O_4$ Nanowire@$NiCo_2O_4$ Nanosheet Core/Shell array.[39, 40] Specifically, the total free energy in the system was reduced by eliminating the surface energy associated with unsatisfied bonds of the nanocrystallines through the bonding between the particles. In our experiments, on the one hand, $CuCo_2O_4$ nanowire acts as the backbone to guide the self-assembly of $NiCo_2(OH)_6$ (the precursor of $NiCo_2O_4$) in aqueous solution during the co-electrodeposition processes. On the other hand, the "oriented attachment" can guide the oriented growth of the nanoparticles. Nanoparticles can attach to the surface of $CuCo_2O_4$ to decrease surface energy due to their high surface energy and thermodynamics instability. As shown in Figure 2e, the nanoparticles attached on the surface of $CuCo_2O_4$ gradually grew into the nanosheets with the increase of the co-electrodeposition time. As shown in Figure S3, the nanowires would be covered completely by $NiCo_2O_4$ finally.

The hierarchical $CuCo_2O_4$ nanowire@$NiCo_2O_4$ nanosheet core/shell arrays on Ni foam were used as electrode to investigate the pseudocapacitive performance. All electrochemical tests were carried out in a three electrode (a saturated calomel electrode was used as the reference electrode and a platinum electrode as the counter electrode) electrochemical cell containing 3 M KOH aqueous solution as the electrolyte. At first, in order to exclude the contribution of the substrate, the blank measurement of Ni foam was carried out and the CVs curve was shown in Figure S4. For comparison, $CuCo_2O_4$ nanowire arrays on Ni foam were also investigated by the same method. Figure 4a shows the cyclic voltammetry (CV) performance of $CuCo_2O_4$ and $CuCo_2O_4$ nanowire@$NiCo_2O_4$ nanosheet core/shell arrays grown on Ni foam with a scan rate of 5 mV s^{-1}. The non-rectangular shape of the CV curve means that the capacitance is from the Faradaic reactions of electrode materials.[41] Apparently, a pair of redox peaks at 0.21 and 0.34 V are observed for the bare $CuCo_2O_4$ electrode, which are due to the Co^{3+} /Co^{4+} and Cu^{2+}/Cu^{+} transitions associated with anions OH^-. A similar CV curve was observed for the $CuCo_2O_4$ nanowire@$NiCo_2O_4$ nanosheet core/shell arrays. However, the CV curves of the hybrid electrodes significantly expanded compared to the bare $CuCo_2O_4$ electrode, indicating that the $CuCo_2O_4$@$NiCo_2O_4$ electrode has a larger capacitance.[42] The phenomena can be attributed to the deposition of $NiCo_2O_4$ nanosheets which enhanced the mass loading and enlarged the surface area of the active materials.

Figure 4b shows the charge/discharge curves of the $CuCo_2O_4$ electrode and $CuCo_2O_4$@$NiCo_2O_4$ hybrid electrode within the potential range from 0 to 0.42 V at the current density of 10 mA cm^{-2}. The specific capacitance of $CuCo_2O_4$@$NiCo_2O_4$ hybrid electrode is calculated to be 2029 F g^{-1}, which is higher than the pristine $CuCo_2O_4$ electrode (1512 F g^{-1}). Figure 4c shows the typical CV curves of the $CuCo_2O_4$@$NiCo_2O_4$ hybrid electrode within the potential range of 0−0.5 V at various scan rates. As the scan rate increases, the anodic peak potential shifts to a higher potential while the cathodic peak potential shifts to a lower potential. It may be resulted from the polarization effect of the electrode.[43] Figure 4d shows the charge/discharge curves of the $CuCo_2O_4$@$NiCo_2O_4$ hybrid electrode at different current densities ranging from 2 to 30 mA cm^{-2}. According to the equation (3), the specific capacitances of the hybrid electrode are calculated to be 2517, 2373, 2029, 1767 and 1551 F g^{-1} at the current densities of 2, 5, 10, 20 and 30 mA cm^{-2}, respectively. Obviously, the specific capacitance decreases with the current density increasing. For comparison, the specific capacitances of pristine $CuCo_2O_4$ electrode under the same pretreatment were also tested. As shown in Figure 5a, the specific capacitances of the pristine $CuCo_2O_4$ electrode are calculated to be 2150, 1794, 1512, 1158 and 923 F g^{-1}at the current densities of 2, 5, 10, 20 and 30 mA cm^{-2}, respectively. Evidently, the hybrid electrode shows a much higher specific capacitance compared to the pristine one. Furthermore, when the current density increases from 2 to 30 mA cm^{-2}, the specific capacitance of the hybrid electrode still retains 1551 F g^{-1}(61.6% of the highest value at 2 mA cm^{-2}), which is much higher than the pristine one (42.9% of the highest value), indicating much better rate performance of the hybrid structures.

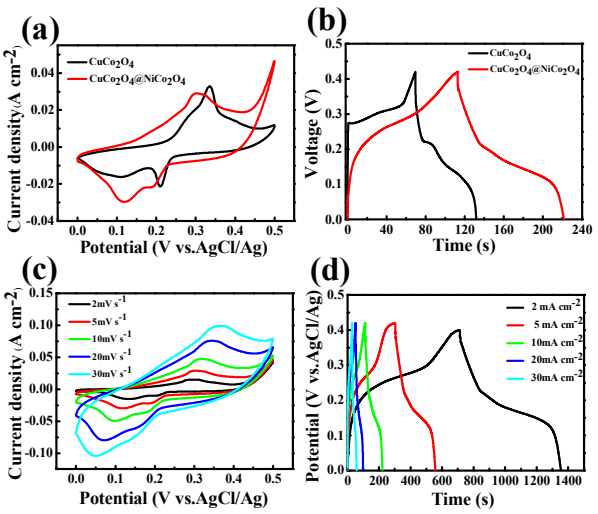

Figure 4. (a) CV curves of the $CuCo_2O_4$ and $CuCo_2O_4$@$NiCo_2O_4$ hybrid electrodes at a scan rate of 5 mV s^{-1}. (b) Charge/discharge curves of the $CuCo_2O_4$ and $CuCo_2O_4$@$NiCo_2O_4$ hybrid electrodes at a current density of 10 mA cm^{-2}. (c) CV curves of the $CuCo_2O_4$ and $CuCo_2O_4$@$NiCo_2O_4$ hybrid electrodes at various scan rates. (d) Charge/discharge curves of the $CuCo_2O_4$@$NiCo_2O_4$ hybrid electrodes at different current densities.

The cycling stability is another important factor for the application of supercapacitors.[44] The cycling performance of $CuCo_2O_4$ electrode and the $CuCo_2O_4$@$NiCo_2O_4$ hybrid electrode were tested after activation at the current density of 10 mA cm^{-2}. The galvanostatic charge−discharge measurements were conducted in the potential range of 0-0.42 V with 3M KOH as the electrolyte. As shown in Figure 5b, the specific capacitance of the hybrid electrode retains 1548 F g^{-1} which is 76% of the original value after 4500 cycles, while the specific capacitance of the pristine $CuCo_2O_4$ electrode retains 1153 F g^{-1} (75.8% of the original value after the same cycles) at the same current density. That indicates the process of electrochemical deposition increases the specific capacitance while does not affect the cycling stability, which can be further proved by the SEM image, as shown in Figure 5d, of $CuCo_2O_4$@$NiCo_2O_4$ hybrid electrode after 4500 cycles. The 3D core/shell nanostructure only changes slightly after 4500 cycles compared with the SEM images before 4500 cycles, almost same as the original one. The corresponding areal capacitances were calculated and shown in Figure S5.

To further explain the excellent electrochemical properties of $CuCo_2O_4$@$NiCo_2O_4$ hybrid electrode, EIS was carried out in a three electrode system. The corresponding impedance Nyquist plots of the pristine $CuCo_2O_4$ electrode and $CuCo_2O_4$@$NiCo_2O_4$ hybrid electrode are shown in Figure 5c, and the inset shows the blowup image at high frequency. In the low frequency region, where the slope of the curve represents the Warburg impedance, the hybrid electrode shows a more ideal straight line, suggesting more efficient electrolyte and proton diffusion. This result can be attributed to the typical 3D core/shell nanostructure which enlarges the specific surface area and shortens the diffusion distance between the electrolyte and electrode. In the high frequency region, the intersection of the curve at real part Z' indicates the bulk resistance of the electrochemical system, and the semicircle of the Nyquist diagram represents the Faradic reaction during the charge/discharge processes. From Figure 5c, the $CuCo_2O_4$@$NiCo_2O_4$ hybrid electrode shows a low bulk resistance and charge-transfer resistance compared to the pristine $CuCo_2O_4$ electrode. The EIS data indicates that the electrodeposition of $NiCo_2O_4$ nanosheets improves the electrical conductivity of the hybrid electrode, resulting in enhanced electrochemical properties compared to the bare $CuCo_2O_4$.

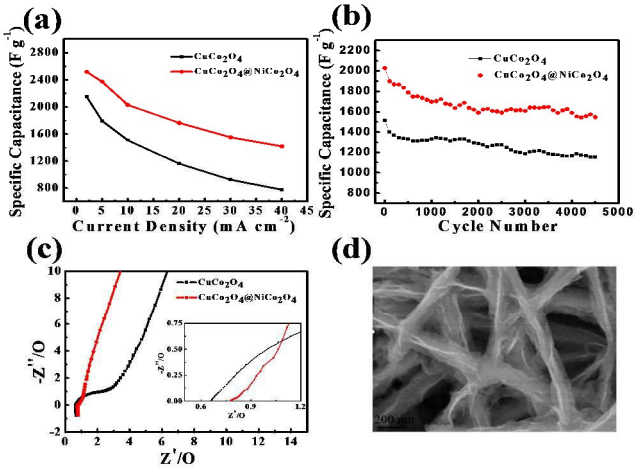

Figure 5. (a) Specific capacitances of $CuCo_2O_4$ and $CuCo_2O_4$@$NiCo_2O_4$ hybrid electrodes at different current densities. (b) Long-term cycling stability of $CuCo_2O_4$ and $CuCo_2O_4$@$NiCo_2O_4$ hybrid electrodes at a current density of 10 mA cm^{-2}. (c) Impedance Nyquist plots of the hybrid structure and the pure $CuCo_2O_4$ nanowires on nickel foam at an open circuit potential. (d) SEM image of the $CuCo_2O_4$ nanowire@$NiCo_2O_4$ nanosheet core/shell arrays after 4500 cycles.

Table 1 summaries some state-of-the-art results about the different materials for supercapacitors. As a matter of fact, our results are superior to other electrode system. Several contributing factors result in the high specific capacitance, good rate capability and excellent cycling stability of the $CuCo_2O_4$@$NiCo_2O_4$ core/shell arrays. First, the $CuCo_2O_4$ nanowires were directly grown on Ni foam with a robust adhesion. The obtained samples were used as the electrode without using polymer binders, which enhanced the utilization of electrode materials and improved the ion diffusion and electron transport. Second, the $NiCo_2O_4$ nanosheets synthesized via the electrodeposition process were well wrapped on the porous $CuCo_2O_4$ nanwires, which maintained the cycling stability of the core/shell structure during the charge/discharge process. Third, the porous $CuCo_2O_4$ nanowires served as the "core" owing to its outstanding electrical conductivity, while the ultrathin $NiCo_2O_4$ nanosheets served as the "shell" with a high theoretical capacity enabled by the multiple oxidation states for the redox reaction. Therefore, the $CuCo_2O_4$@$NiCo_2O_4$ core/shell structures were able to realize the outstanding supercapacitive performance.

Materials	Structure	Capacitance	Reference
$NiCo_2O_4$@$NiCo_2O_4$	Core/Shell Nanaoflake arrays	2.20 F cm^{-2} (5 mA cm^{-2})	36
$NiCoS_x$	Nanosheets	1418 F g^{-1} (5 A g^{-1})	20
Co_3O_4	Nanowires	754 F g^{-1} (2 A g^{-1})	25
$NiCo_2O_4$@MnO_2	Core/Shell Nanowire arrays	2.24 F cm^{-2} (2 mA cm^{-2})	31
$CuCo_2O_4$@$NiCo_2O_4$	Core/Shell	2.59 F cm^{-2} (10 mA cm^{-2}), 2029 F g^{-1} (7.8 A g^{-1})	This work

Table 1. The electrochemical capacitances of different electrode materials.

4. Conclusions

In conclusion, we have developed an easy and effective strategy to prepare the unique hierarchical core/shell structure of $CuCo_2O_4$ NWs@$NiCo_2O_4$ NSs on Ni foam, which can be directly used as the electrode for supercapacitors. The as-prepared electrode shows good electrochemical performance. The capacitance is calculated to be 2029 F g^{-1} (2.59 F cm^{-2}) when the current density is 10 mA cm^{-2}. Furthermore, when the current density increases from 2 to 30 mA cm^{-2}, the specific capacitance of the hybrid electrode retains 1551 F g^{-1} (61.6% of the highest value). Besides, the hybrid electrode still delivers a high specific capacitance of 1548 F g^{-1} (76% of the original value) after 4500 cycles with a current density of 10 mA cm^{-2}. Its outstanding electrochemical performance takes advantages of the material system which have high theoretical capacitance and 3D core/shell nanostructures which are able to shorten the diffusion distance between the electrolyte and electrode, enlarge the specific surface area and offer more active materials. Therefore, the $CuCo_2O_4$ nanowire@$NiCo_2O_4$ nanosheet core/shell arrays may serve to be a promising candidate as electrode material for supercapacitors.

Acknowledgements

We gratefully acknowledge financial support from the National Natural Science Foundation of China (Grant nos.11274107 and 61204109), the Program for New Century Excellent Talents in University (NCET-13-0185), and the Foundation for the authors of National Excellent Doctorial Dissertation of China (201318).

References

1 J. Li, X. Wang, Q. Huang, S. Gamboa and P. J. Sebastian, *Journal of Power Sources.*, 2006, **158**, 784-788.
2 D. Kalpana, N. G. Renganathan and S. Pitchumani, *Journal of Power Sources.*, 2006, **157**, 621-623.
3 C. Kim, Y. O. Choi, W. J. Lee and K. S. Yang, *Electrochimica Acta.*, 2004, **50**, 883-887.
4 K. H. An, W. S. Kim, Y. S. Park, H. J. Jeong, Y. C. Choi, J.-M. Moon, D. J. Bae, S. C. Lim and Y. H. Lee, *American Institute of Physics.,* 2001, **590**, 241-244.
5 C. Liu, Z. Yu, D. Neff, A. Zhamu and B. Z. Jang, *Nano letters.*, 2010, **10**, 4863-4868.
6 J. R. Miller, R. A. Outlaw and B. C. Holloway, *Science*, 2010, **329**, 1637-1639.
7 Y. Wang, Z. Shi, Y. Huang, Y. Ma, C. Wang, M. Chen and Y. Chen, *The Journal of Physical Chemistry C.*, 2009, **113**, 13103-13107.
8 D. Yu and L. Dai, *The Journal of Physical Chemistry Letters.*, 2010, **1**, 467- 470.
9 T. Cottineau, M. Toupin, T. Delahaye, T. Brousse and D. Bélanger, *Applied Physics A.*, 2005, **82**, 599-606.
10 A. L. M. Reddy and S. Ramaprabhu, *The Journal of Physical Chemistry C.*, 2007, **111**, 7727-7734.
11 S. Vijayakumar, A. K. Ponnalagi, S. Nagamuthu and G. Muralidharan, *Electrochimica Acta.*, 2013, **106**, 500-505.
12 L. Cao, F. Xu, Y. Y. Liang and H. L. Li, *Advanced materials.*, 2004, **16**, 1853-1857.
13 C. C. Hu, J. C. Chen and K. H. Chang, *Journal of Power Sources.*, 2013, **221**, 128-133.
14 U. M. Patil, K. V. Gurav, V. J. Fulari, C. D. Lokhande and O. S. Joo, *Journal of Power Sources.*, 2009, **188**, 338-342.
15 L. Zhang, H. B. Wu and X. W. Lou, *Chemical communications.*, 2012, **48**, 6912-6914.
16 W. Chen, C. Xia and H. N. Alshareef, *ACS Nano.*, 2014, **8**, 9531-9541.
17 B. Hu, X. Qin, A. M. Asiri, K. A. Alamry, A. O. Al-Youbi and X. Sun, *Electrochimica Acta.*, 2013, **100**, 24-28.
18 S. K. Meher and G. R. Rao, *The Journal of Physical Chemistry C.*, 2011, **115**, 15646-15654.
19 Y. Wang, Z. Zhong, Y. Chen, C. T. Ng and J. Lin, *Nano Research.*, 2011, **4**, 695-704.
20 Z.-S. Wu, W. Ren, L. Wen, L. Gao, J. Zhao, Z. Chen, G. Zhou, F. Li and H.-M. Cheng, *ACS Nano.*, 2010, **4**, 3187-3194.
21 X.-h. Xia, J.-p. Tu, Y.-q. Zhang, Y.-j. Mai, X.-l. Wang, C.-d. Gu and X.-b. Zhao, *RSC Advances.*, 2012, **2**, 1835-1841.
22 G. Zhang, T. Wang, X. Yu, H. Zhang, H. Duan and B. Lu, *Nano Energy.*, 2013, **2**, 586-594.
23 F. Bao, Z. Zhang, X. Liu and X. Zhao, *RSC Advances.*, 2014, **4**, 38073.
24 F. Bao, X. Wang, X. Zhao, Y. Wang, Y. Ji, H. Zhang and X. Liu, *RSC Adv.*, 2014, **4**, 2393-2397.
25 H. Chen, J. Jiang, L. Zhang, T. Qi, D. Xia and H. Wan, *Journal of Power Sources.*, 2014, **248**, 28-36.
26 J. Du, G. Zhou, H. Zhang, C. Cheng, J. Ma, W. Wei, L. Chen and T. Wang, *ACS applied materials & interfaces.*, 2013, **5**, 7405-7409.
27 Q. Wang , J. Xu, X. Wang, B. Liu, X. Hou, G. Yu, P. Wang, D. Chen and G. Shen, *ChemElectroChem.*, 2014, **1**, 559-564.
28 S. G. Mohamed, C. J. Chen, C. K. Chen, S. F. Hu and R. S. Liu, *ACS applied materials & interfaces.*, 2014, **6**, 22701-22708.
29 L.-B. Kong, C. Lu, M.-C. Liu, Y.-C. Luo, L. Kang, X. Li and F. C. Walsh, *Electrochimica Acta.*, 2014, **115**, 22-27.
30 L. Bao, J. Zang and X. Li, *Nano letters.*, 2011, **11**, 1215-1220.
31 L. Huang, D. Chen, Y. Ding, Z. L. Wang, Z. Zeng and M. Liu, *ACS applied materials & interfaces.*, 2013, **5**, 11159-11162.
32 G.-R. Li, Z.-L. Wang, F.-L. Zheng, Y.-N. Ou and Y.-X. Tong, *Journal of Materials Chemistry.*, 2011, **21**, 4217.
33 Q. Qu, Y. Zhu, X. Gao and Y. Wu, *Advanced Energy Materials.*, 2012, **2**, 950-955.
34 A. Vu, Y. Qian and A. Stein, *Advanced Energy Materials.*, 2012, **2**, 1056-1085.
35 Y. Qian, A. Vu, W. Smyrl and A. Stein, *Journal of the Electrochemical Society.*, 2012, **159**, A1135-A1140.
36 X. Liu, S. Shi, Q. Xiong, L. Li, Y. Zhang, H. Tang, C. Gu, X. Wang and J. Tu, *ACS applied materials & interfaces.*, 2013, **5**, 8790-8795.
37 Y. Qian, I. M. Ismail and A. Stein, *Carbon.*, 2014, **68**, 221-231.
38 Z. Yu, Z. Cheng, S. R. Majid, Z. Tai, X. Wang and S. Dou, *Chemical communications.*, 2015, **51**, 1689-1692.
39 L. Q. Mai, F. Yang, Y. L. Zhao, X. Xu, L. Xu and Y. Z. Luo, *Nature communications.*, 2011, **2**, 381.
40 M. Niederberger and H. Colfen, *Physical chemistry chemical physics : PCCP.*, 2006, **8**, 3271-3287.
41 H. Wang, Q. Gao and L. Jiang, *Small.*, 2011, **7**, 2454-2459.
42 J. W. Lee, A. S. Hall, J.-D. Kim and T. E. Mallouk, *Chemistry of Materials.*, 2012, **24**, 1158-1164.
43 J. W. Lee, T. Ahn, J. H. Kim, J. M. Ko and J.-D. Kim, *Electrochimica Acta.*, 2011, **56**, 4849-4857.
44 H. Wang, Y. Wang, Z. Hu and X. Wang, *ACS applied materials &*

interfaces., 2012, **4**, 6827-6834.